Global Miocene tectonics and regional sandstone-style uranium mineralization

Yinhang Cheng[a,b,c,*], Shaoyi Wang[b,c], Ruoshi Jin[b,c], Jianguo Li[b,c], Cong Ao[b,c], Xueming Teng[b,c]

[a] China University of Geosciences (Beijing), Beijing 100083, China
[b] Tianjin Center, China Geological Survey, Tianjin 300170, China
[c] Laboratory of Non-fossil Energy Minerals, Tianjin Center of China Geological Survey, Tianjin 300170, China

ABSTRACT

The formation of sandstone-style uranium deposits are significantly controlled by the latest tectonic uplift events, especially those generated in an open system by the infiltration of meteoritic water. This study explores the spatiotemporal relationship between global Miocene tectonics and sandstone-style uranium deposits to evaluate the link between tectonic uplift and metallogenic ages. In general, modern landforms were shaped by diverse global tectonic events that began in the Middle and Late Miocene. This includes the formation of continental-scale faults and fold belts, including the uplift of the three broadly contemporaneous ranges, the Alpine–Himalayan Belt, the Cordillera, and the East African Rift. These events were accompanied by intense magmatic activity, as well as an increase in the spreading rates of oceanic ridges and higher sedimentation rates in the Pacific, Indian, and Atlantic oceans. Modern global climate patterns are a direct consequence of these Miocene tectonic events. Studies on sandstone-style uranium deposits report that though their stratigraphic ages extend from the Proterozoic to the Cenozoic, they notably occur from the Late Mesozoic to the Neogene. Uranium mineralization ages are concentrated between 20 and 0.1 Ma, clustering mainly in the Miocene although remobilizations are known to have occurred subsequently, some even in the Holocene. Global tectonics in the Miocene, between 20 and 5 Ma, resulting in the regional uplift of mountain ranges and continental tilts, may have exerted significant control over the migration directions of uranium-bearing fluids that formed these sandstone-style uranium deposits. Climate patterns in the Miocene, specifically subtropical high-pressure belts on both sides of the equator controlled the creation of arid and semi-arid areas, creating characteristic rainfall patterns which would also have influenced the spatial distribution of these uranium deposits. Thus, the spatiotemporal characteristics of most sandstone-style uranium deposits in the world were controlled by global tectonics in the Miocene that uplifted mountain ranges and tilted continents, generating subtropical high-pressure belts and the Asian high pressure region. In addition to new ideas adding greater research value to the study of global sandstone-style uranium mineralization, this paper also provides a new exploration indicator for sandstone-style uranium deposits.

1. Introduction

Sandstone-style uranium deposits in this paper are defined as basal channel, tabular and roll front deposits that form by the infiltration of meteoric or groundwater enriched in uranium (Cuney, 2013). The linkage between Miocene tectonics and the infiltration of uranium-rich meteoric water that precipitates to form sandstone-style uranium deposits remains vague. The characteristics of hydrogenic, dynamic, and open system mineralization have generated considerable uncertainty, resulting in a wide span of deposit ages (Wang, 2002; Xia, 2015; Jaireth et al., 2016; Zhang, 2016; Hall et al., 2017; Jin et al., 2017). In China,

the Sunjialiang deposit ages range from 20 to 8 Ma (Xia, 2015) and those from Ningdong range from 11 to 4 Ma (Wang et al., 2018); the Qianjiadian ore deposits have a longer age range, from 53 to 3 Ma (Zhang et al, 2005; Zhao et al., 2018). The Kazakhstan Chu–Sarysu deposit ages range from the Oligocene to the Quaternary, and in the USA, the ages of the Grants deposit in New Mexico range from 13 to 4 Ma (Jaireth et al., 2016), while those from Texas range from 5.07 to 0.15 Ma (Hall et al., 2017). The ages of uranium deposits coincide with Cenozoic tectonic events, but are significantly younger than their strata ages, which range from the Proterozoic to the Cenozoic (Jin et al., 2017; Wang et al., 2017a). Consequently, the precise dating of

sandstone-style uranium deposits is very difficult and remains an unresolved research problem due to the small quantity of uranium available for *in situ* dating, its mineralogical complexity which includes uranium oxides mixed with coffinite or ningyoite, and its frequent alteration either by lead loss or from radon loss by alpha recoil because of the small size of uranium minerals.

The significance of tectonics, climate, and fluids on sandstone-style uranium deposits is widely recognized (e.g., Liu et al., 2009a; Jiao et al., 2015; Jaireth et al., 2016; Sheahan et al., 2016; Zhang, 2016; Jin et al., 2016; Hall et al., 2017; Wang, 2017b). Most sandstone-style uranium deposits formed in arid and semi-arid environments (Wang et al., 2017a), and continental tilt belts (Liu et al., 2009a; Wang et al., 2017a). Studies suggest that their formation may have been controlled by Cenozoic tectonics (Chen et al., 2010a) and neotectonics (Zhang, 2016), Neogene synsedimentary tectonic activity (Zhou et al., 2017), monoclinal structural control (Liu et al., 2009a), and intra-basin uplift (Jin et al., 2016). Complex mineralization ages, in addition to their hydrogenic and dynamic characteristics suggest that uranium may have been concentrated in veins and subsequently leached (Placzek et al., 2016; Domnicka et al., 2018). Uranium mineralization is most likely a continuous process; it is strongly influenced by regional tectonics, and may persist till today. However, questions regarding when and which events most influenced uranium mineralization in the world remain unanswered.

In this study, we assemble evidence from global Miocene tectonics that reshaped the modern global landscape (Fig. 1), forming major river systems (Harrison et al., 1992; Gradstein et al., 2004; Clark and Bilham, 2008; Potter and Szatmari, 2009, 2015; Bracciali et al., 2015) and modern geomorphology, and formed today's climate which is very similar to that of the Miocene (Xiao et al., 2014; Wang et al., 2017a); we then explore their relationship with regional sandstone uranium mineralization on Earth. Our study reveals that the modern mountain ranges that were formed by major global tectonic events in the Miocene controlled the development of the three main metallogenic belts for sandstone-style uranium deposits (Fig. 2), the Alpine–Himalayan Belt, the Cordillera Belt, and the East African Rift Belt, respectively. The mineralization ages of sandstone-style uranium deposits are clustered from the Miocene to the Pleistocene, indicating continuous mineralization and multiple remobilizations. The development of subtropical high-pressure belts (SHPBs) on both sides of the equator controlled the formation of arid and semi-arid areas as well as regional rainfall patterns, influencing the distribution of sandstone-style uranium deposits.

2. Global tectonics in the Miocene

2.1. Tectonic setting

The world's two longest mountain chains—the 13,000 km Alpine–Himalayan Belt in the Eurasian plate and the 16,000 km

Cordillera in the western Americas, respectively—and the 6400 km East African Rift, together form the largest intra-continental rifting belts. These three ranges and the tilts along these ranges control the distribution of most sandstone-style uranium deposits in the world (Fig. 2). Subduction, collision, and extension are the three types of interactions between two plates; any of them can raise continental elevations and back-tilt entire continents. These mountain ranges are focal points of study for the dynamic mineralization of sandstone-style uranium deposits. Epeirogenic uplift increasing the average elevation of continents was also proposed as an important factor leading to local climate change (Eyles, 1996; Guo, et al., 2002).

The Alpine–Himalayan Belt contains many complex sutures that started in the Permian from successive collisions of Gondwana fragments, and which culminated with the impact of Africa, Arabia, and India during the Cenozoic (Potter and Szatmari, 2015). These sutures closed the Tethyan Ocean and the residual Mediterranean, Black, Caspian, and Aral Seas in Europe, forming a complex of collisional mountains, wide plateaus, and large intermountain basins along the chain, namely the Himalayas, the Tibetan Plateau, and the Tarim Basin in Asia.

The Cordillera mountains occur along the eastern Pacific Ocean (Fig. 2) and have a completely different tectonic setting from that of the Alpine–Himalayan Belt. Most were formed due to the collision of the westward-moving American plates over subducting Pacific Ocean lithosphere (Sclater et al., 1985; Potter and Szatmari, 2015). In the Miocene, both the American plates moved westward consuming old, cold, and deep Pacific lithosphere. These plates subsequently contacted young, hot, and shallow Pacific lithosphere, which resisted subduction and accelerated the rise of the Andean and Cordilleran mountains (Potter and Szatmari, 2015).

The East African Rift is the largest intra-continental rifting belt east of the African plate. It lies between the African and Indian plates, and formed as a result of tension between them. The whole area was uplifted between the Late Oligocene and the Miocene, during which time, the mantle beneath the Earth's crust rose and was diverted, resulting in great tension and the formation of a rift valley. The depression of the East African Rift began in the Oligocene. Movement along the main fault and tectonic uplift occurred in the Miocene, and the period of large strike-slip movement lasted from the Pliocene to the Quaternary (Guillocheau et al., 2018).
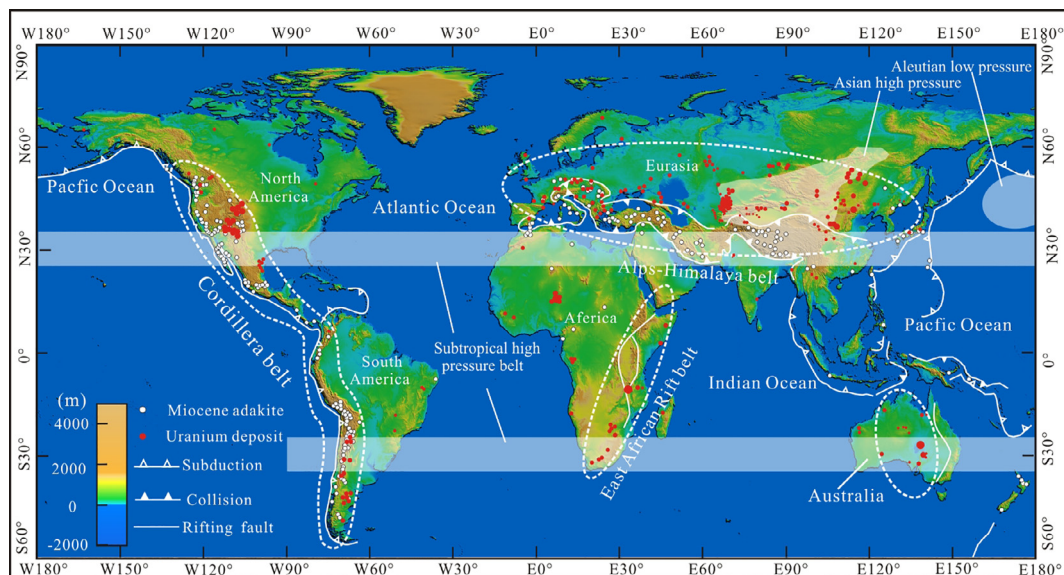
3. 2. Global tectonics in the Miocene

We synthesize evidence from global magmatic activity, faults and fold belts, and the relationships between tectonic uplift and mineralization changes during the dynamic Miocene Epoch (23.0 to 5.3 Ma; Fig. 1) and demonstrate how they facilitated the mineralization of sandstone-style uranium deposits.

3.0.1. Active magmatism

In the Miocene, widespread volcanism occurred not only along mid-oceanic ridges and ocean–continent convergent margins, but also on the continents and in some intra-plate regions. Global occurrences of Cenozoic magmatic rocks and Miocene adakites assessed in this study (Fig. 3) indicate that igneous rocks in the Cenozoic include andesite and basalt from convergent margins, continental rifts and ocean island settings, in addition to adakite; they are mainly distributed along the Alpine–Himalayan suture (formed by continent–continent collisions), the circum-Pacific magma arc (volcanic and subduction-related), and the East African Rift (continental rift) (Potter and Szatmari, 2015; Guillocheau, et al., 2018). During the Cenozoic, magmatic activity either started or intensified along these plate suture zones, achieving a peak in the Miocene (Fig. 3a), as did the formation of adakite, indicating strong crustal compression and thickening leading to regional tectonic uplift (Fig. 3b). The distribution of Miocene adakite along the

Fig. 1. Epochs, stages, and ages of the Cenozoic (Gradstein et al., 2004).

Fig. 2. Digital elevation model map and global distribution of sandstone-style uranium deposits (Jin et al., 2016, 2017; Wang et al., 2017a) and Miocene adakite (Ma et al., 2017) showing Cenozoic faults (after Coltice et al., 2017); red dots are scaled to the relative size of the resource; dotted lines show sandstone-style uranium deposit belts. (For interpretation of the references to colour in this figure legend, the reader is referred to the web version of this article.)

Alpine–Himalayan Belt and the Cordillera has spatial characteristics similar to those of sandstone-style uranium deposit mineralization belts (Fig. 2). Continental rift volcanic rocks display a bimodal suite in the East African Rift during the Paleogene and in the Miocene (Guillocheau, et al., 2018); sandstone-style uranium deposits are also distributed along the East African Rift (Fig. 2). Magmatic rocks from the west and east of the Alpine–Himalayan Belt have ages of 15–5 Ma (Lustrino and Wilson, 2007) and 26–7 Ma (Wu et al., 2015); those from the Cordillera have ages of 16–0.6 Ma (Guillocheau, et al., 2018), and those from the Andes have ages of 15–10 Ma (Armijo et al., 2015). The ages of these magmatic rocks are mostly Middle to Late Miocene, a relic of the increased tectonic activity and significant continental tilts which developed at that time (Fig. 2), providing tectonic conditions favorable for fluid migration and the formation of sandstone-style uranium deposits.
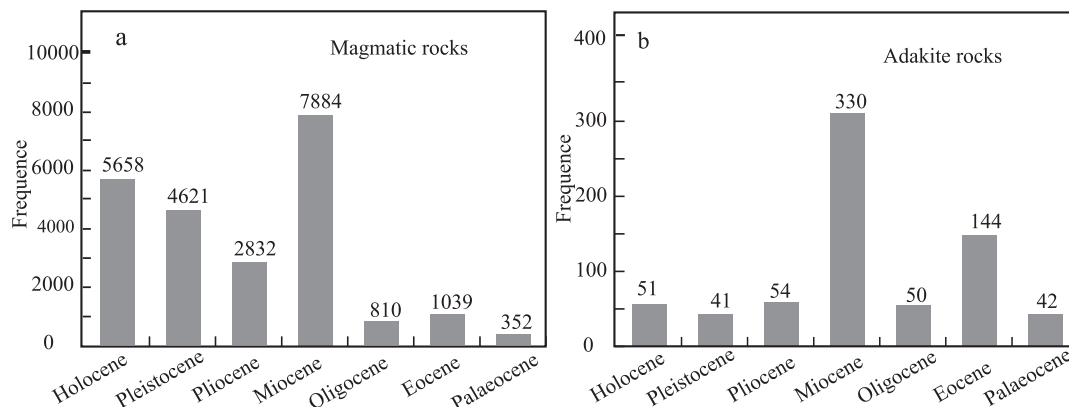
3.0.2. The last regional tectonic uplift in the Miocene

Tectonic uplift plays an important role in the mineralization of sandstone-style uranium deposits (Jin et al., 2016), especially the most recent tectonic events. The thermo-tectonic events of the three sandstone-style uranium deposit mineralization belts indicate that these mountain ranges experienced rapid uplift in the Middle and Late Miocene (Fig. 4). The last uplift ages of the Alpine–Himalayan epeirogenic
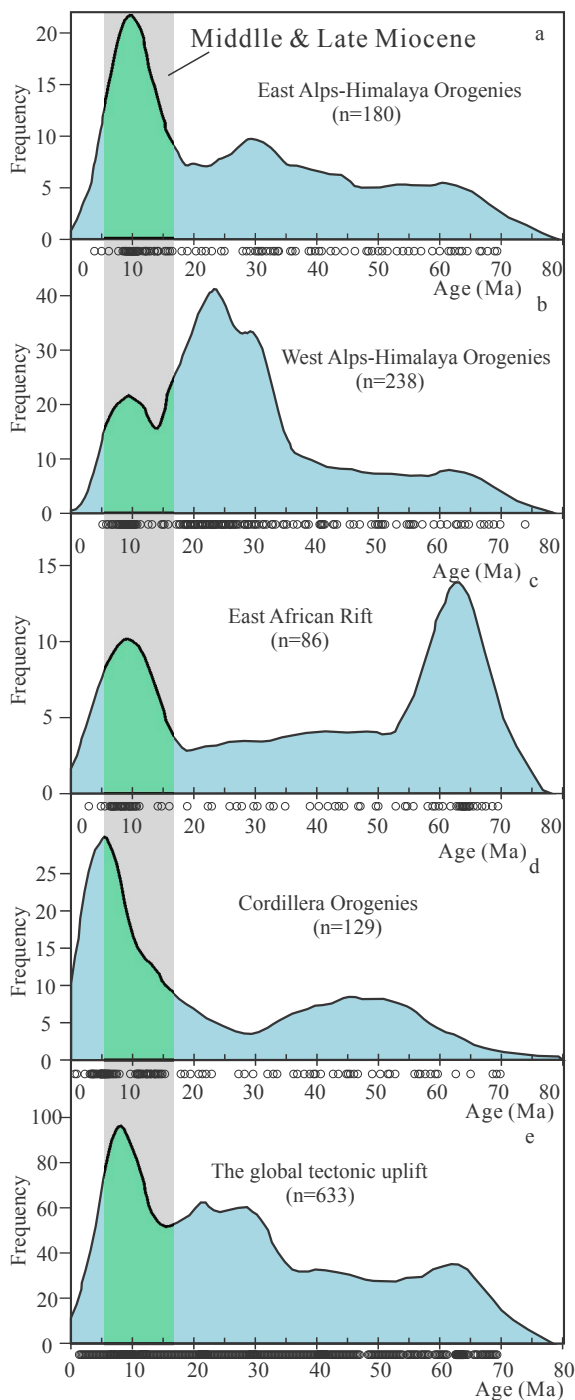
belt are 20–5 Ma in the eastern part (Fig. 4a) and 14–4 Ma in the western part (Fig. 4b), the uplift ages of the East African Rift are 16–5 Ma (Fig. 4c), and the uplift ages of Cordillera epeirogenic belt are 25–4 Ma (Fig. 4d). The thermo-tectonic data from these three ranges indicate that their last tectonic uplift occurred at 15–5 Ma (Fig. 4e). In addition, the age of the sandstone-style uranium metallogenic region of Australia is ~ 12 Ma (Van Ufford and Cloos, 2005) with the last tectonic uplift ages at the southeastern margin being 50–25 Ma (Gleadow et al., 2002).

3.0.2.1. Alpine–himalayan epeirogenic uplift

The eastern and western regions of the Alpine–Himalayan orogenic belt are different. In the eastern part, the last regional tectonic uplift of the north Tibetan Plateau occurred mostly from 20 to 5 Ma (Li et al., 2011; Wang, 2013), as confirmed by apatite and zircon fission-track data from Qilian (10 Ma), the Tianshan Mountains (24–12 Ma), the Longmen Mountains (13–5 Ma), the Liupan Mountains (8 Ma), the Kyrgyz Range (11 Ma), Altyn Tagh (15 Ma), Gobi–Altay (5 Ma) (Wang, 2013), the Songliao area (16 Ma) (Cheng et al., 2018), and Kaghan Valley, Pakistan (24–5 Ma) (Wilke et al., 2012); this is also corroborated by continuous aeolian deposits with ages from 22 to 6.2 Ma, estimated from palaeomagnetic measurements and fossil evidence (Guo et al., 2002). Southern Kazakhstan, since the Oligocene, has been

Fig. 3. Age distribution histograms of (a) global magmatic rocks and (b) adakite rocks during the Cenozoic (modified after Liu et al., 2017a).

Fig. 4. Global thermo-tectonic events indicated by kernel density estimates of fission-track ages in the Alpine–Himalayan Belt, the Cordillera, and the East African Rift, with $P(\chi^2) > 5\%$; (a) after Wang et al. (2011), Wilke et al. (2012), Wang (2013), Cheng et al. (2015), Lin et al. (2015), and Vetrov et al. (2016); (b) after Thomson and Stuart (1994), Bojara et al. (1998), Barbarand et al. (2001), Juez-Larré et al. (2002), Balestrieri et al. (2013), Esteban et al. (2013), Wauschkuhn et al. (2015), Karaoğlan et al. (2016), and Ring et al. (2017); (c) after Foster and Gleadow (1992), Wagner et al. (1992), Balestrieri et al. (2005, 2016), Tinker et al. (2008), Brown et al. (2014), Jelinek et al. (2014), Wildman et al. (2015), and Piedrahita et al. (2017); (d) after Spiegel et al. (2007), Vera et al. (2015), Enkelmann et al. (2017), Piquer et al. (2017), Balestrieri et al. (2017), and Martínez et al. (2017); (e) from all of the above.

subjected to compression due to the rapid Arabia-Turan oblique convergence in the south and collision with the Indian plate in the southeast; in the Neogene, this convergence reactivated and reversed the

Permo-Mesozoic faults responsible for the uplift of the Karatau Mountains (Lyberis and Manby, 1999). In the western Alpine–Himalayan orogenic belt, intense tectonic uplift occurred during the Late Oligocene and Early Miocene, with the last uplift taking place during the Middle and Late Miocene (Fig. 4b). For example, the Turkish–Iranian Plateau formed during 20–10 Ma (Faccenna et al., 2006). Other events, such as the drying up of the Tethys during 20–5 Ma because of tectonic uplift, and the closure of the Spain Benitez Strait and Morocco Strait occurred at ~7.2 Ma (Boulton et al., 2016; Liu et al., 2017a).

3.0.2.2. Cordillera epeirogenic uplift

In North and South America, the last Cordillera epeirogenic uplift began in the Miocene and ended in the Pliocene, peaking at the end of the Miocene (Fig. 4d). The uplift of British Columbia occurred at 10 Ma (Farley et al., 2001) accompanied by the Middle and Late Miocene epeirogenic uplift of much of the interior and coastal regions of the southern United States (Dooley et al., 2013). The 10 Ma uplift in the central Andes (Garzione et al., 2008), and the crustal thickening and exhumation beginning at ~12 and ~7 Ma in the Miocene of the Abanico Basin, central Chile (Piquer et al., 2017) are related to the abrupt crustal thickening and uplift of the Andean ranges during 16–3 Ma in South America (Kay and Kay, 2002). High rates of initial tectonic uplift at 10 Ma were estimated for southeast Alaska and southwest Yukon, North America (Enkelmann et al., 2017). Middle to Late Miocene cooling events in the sediment source areas were identified in the Central and Western Cordilleras of Colombia, South America (Piedrahita, et al., 2017), and at the eastern rheological boundary of the Baja California block (Balestrieri et al., 2017) in North America, with fission-track ages of 12–5 Ma.

3.0.2.3. East African rifting uplift

In East Africa, multiple tectonic uplift events occurred during the Middle and Late Miocene. A tectonic uplift event occurred at ~10 Ma in East Africa (Potter and Szatmari, 2015) and the central Africa uplift occurred during the Early Miocene, between 23 and 16 Ma, as confirmed by the stratigraphic record of the basin margins and thermochronological data in Gabon (Walgenwitz et al., 1992). The uplift increased during the Late Miocene to Early Pliocene (11–3 Ma), as confirmed by an increase in the sediment supply in the Ogooué Delta (Mougamba, 1999) and the rifting uplift of central Africa from 10 to 3 Ma (Sakai et al., 2010; Guillocheau et al., 2018). Significant events in northern Africa during the Miocene include the uplift of the Atlas mountains in the Burdigalian in Algeria, and in the Tortonian in Tunisia (Piqué et al., 2002), closing of the Strait of Gibraltar with the drying up of the Mediterranean (Hsü, 1983; Krijsman et al., 1999), erosion of the Rhone and the Nile canyons (Said, 1981; Issawi and Maccauley, 1993), and tectonic uplift and erosion in the Red Sea and Gulf of Aden areas with ages from 25 to 10 Ma (Balestrieri et al., 2005). By the end of the Miocene, much of the landscape of Africa would be easily recognizable as similar to today's (Potter and Szatmari, 2009).

3.0.3. Faults and fold belts in the Cenozoic

Three broadly contemporaneous faults, with tectonic uplift, exhumation, erosion belts, and gradually manifesting continental tilts formed along the Alpine–Himalayan Belt, the Cordillera and the East African Rift ranges during Cenozoic (Fig. 2). The Alpine–Himalayan epeirogenic uplift belt is ~13,000 km long. It formed by continent–continent collision stretching across southern Eurasia, with the rejuvenation of Mesozoic and Paleozoic mountain chains and a regional northeastward continental tilts along these ranges. This orogeny resulted from the Australian, Indian, Arabian, and African Plates impacting the southern Eurasian Plate, as a consequence of the break-up of Gondwana and the northward movement of its fragments over ~120 Ma to finally close the Tethys Ocean in the Early Miocene (Potter and Szatmari, 2015). Many folds and thrust-faulting complexes
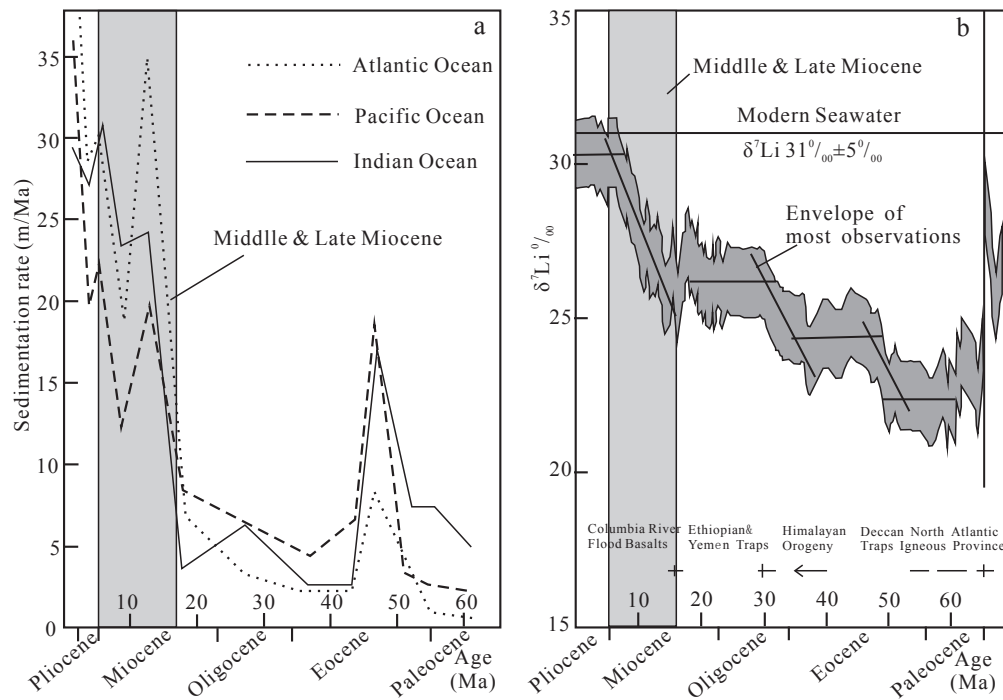
Fig. 5. (a) Rates of oceanic sediment deposition in the Cenozoic (Hsü et al., 1977; Lugli et al., 2015) and (b) the stepwise increase in values of the δ^7Li isotope measured for benthic foraminifera (after Misra and Froelich, 2012).

formed in the compressional environment prevailing along this belt during the Cenozoic (Coltice et al., 2017). The circum-Pacific orogenic belt is a ~26,000 km mountain chain generated by subduction along the margins of the Pacific Ocean plate. The narrow mountains of the South American Cordillera were produced near the coast, with continental tilts eastward to the southern Atlantic Ocean while continental tilts in North America are directed eastward, away from its western marginal mountain ranges and towards the northern Atlantic Ocean. The East African Rift Belt is ~6400 km long; trans-African rifting in the southwestward direction developed in the Miocene. Along the belt, regional continental tilts developed to the southeast and northwest, towards the Indian Ocean and Sahara Desert, respectively.

3.0.4. Clastic deposition in the Miocene

Sedimentation rates (Fig. 5a) greatly increased in the Pacific, Indian, and Atlantic Oceans during the Middle and Late Miocene, and exhibit similar rate changes in the Cenozoic (Hsü et al., 1977; Lugli et al., 2015), indicating synchronous global fluctuations. Sedimentation rates during the Middle and Late Miocene were greater by a factor of 7–8 than in the Oligocene. These changes indicate significantly different modes of continental weathering and an appreciable elevation difference between the mountain ranges and ocean surfaces, since the Miocene was the time in which most ranges in the world developed (Potter and Szatmari, 2015). Many hiatuses occurred and unconformities developed from deep-water scour as a result of Late Cretaceous to Cenozoic global tectonics, as indicated by stable isotope test results (Fig. 5b). Based on many hundreds of benthic foraminifera samples, the stepwise increase in the flooding of hemipelagic mud to the global oceans in the Miocene was well identified at 16 Ma by a sharp rise in δ^7Li$^0/_{00}$ (Misra and Froelich, 2012); this coincided with orogenic activity during the Middle and Late Miocene. Global continental basins also recorded rapid sedimentation in the Neogene (Li et al., 2013) and continuous aeolian deposition in China is indicated by deposition ages from 22 to 6.2 Ma (Guo et al., 2002).

3.0.5. Other tectonic events in the Miocene

Other significant tectonic events that occurred in the Miocene include the rotation of the southwestern and northwestern archipelagos of Japan into their present position between 20 and 13 Ma (Potter and Szatmari, 2009), an increase in the spreading rates of mid-ocean ridges globally in the Middle Miocene (Kominz, 1984), the initiation of polar conveyor belts in response to the opening and closing of seven key oceanic gateways (Potter and Szatmari, 2015), increased sedimentation rates in the Pacific, Indian and Atlantic oceans during the Middle and Late Miocene, and many deep-sea hiatuses and unconformities developing from deep-water scour (Hsü et al., 1977; Lugli et al., 2015).

4. Global climate in the Miocene and the modern world

Climate changes peaked in the Miocene, forming the modern climate patterns that are prevalent today (Zachos et al., 2001; Whipple, 2009; Hoorn et al., 2010; Sakai et al., 2010; Lu and Guo, 2013). Global oceanic and atmospheric cooling events between 15 and 14 Ma, in the Middle Miocene, as inferred from δO^{18} isotopes of benthic foraminifera (Fig. 6) greatly altered the world's temperature regime (Zachos et al., 2001; Miller et al., 2005). The global CO_2 imbalance in the Cenozoic (Fig. 6) indicated that the maximum CO_2 loss occurred at ~16 Ma, followed by cooling at 14.5–13 Ma (Compton and Mallinson, 1996). Many other climatic changes occurred in the Miocene; these changes include (i) the expansion of the Antarctic ice sheet between 15 and 14 Ma (Keller and Barron, 1983) and an increase in mountain glaciation (Eyles et al., 1991), (ii) high oxidization in the oceans in the early Middle Miocene (Norris et al., 2013), (iii) a Middle Miocene climatic optimum at 17.0–14.7 Ma (Hilgren et al., 2012), (iv) the formation of the Asian monsoon in the Middle and Late Miocene (Lu and Guo, 2013; Potter and Szatmari, 2015), and (v) a strong weathering event between 10 and 8 Ma, evidenced from ^{40}Ar/^{39}Ar dating of individual grains of cryptomelane (Carmo and Vasconcelos, 2004), following the development of large rain shadows, along with deserts and loess on continents (Potter and Szatmari, 2015).

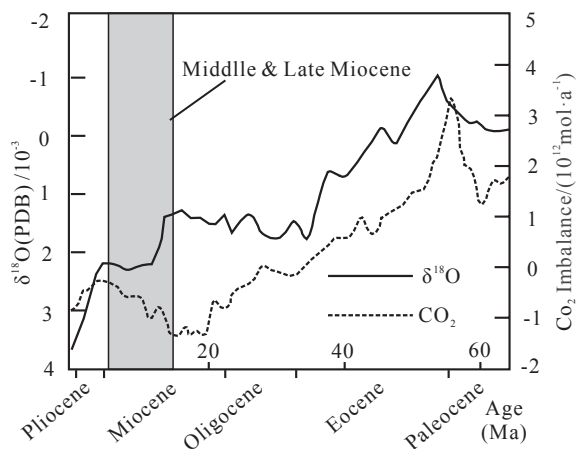The climate during the Miocene (Fig. 7) was similar to today's

Fig. 6. Comparison of the CO_2 imbalance (Compton and Mallinson, 1996) with the $\delta^{18}O$ record (Zachos et al., 2001; Miller et al., 2005) for Cenozoic benthic foraminifera.

(Fig. 8), but differed greatly from that in the Oligocene. In the Miocene, well-defined climate belts stretched from the poles to the equator. Arid and semi-arid areas were mainly distributed in northern and southern Africa, southwestern Eurasia, and middle-west America, with characteristics similar to those of the modern world (Qian et al., 2017). However, Australia was less arid than it is today, possibly influenced by the subtropical high-pressure belt in the southern hemisphere. In the Late Oligocene–Early Miocene, central Australia was farther to the south and yet supported tropical forests (Langford et al., 1995).

5. Relationships among uranium mineralization, tectonic uplift, and climate

5.1. Mineralization ages

Mineralization ages of sandstone-style uranium deposits cover a wide span of time leading to some confusion between primary uranium deposition and multiple remobilizations, in many deposits. In this study, experimental tests were used to study mineralization times. The ages of host units for sandstone-style uranium deposits range from the Proterozoic to the Cenozoic, although 80% of their worldwide occurrences are concentrated in the Mesozoic and Cenozoic (Wang et al., 2017a). Ages of sandstone-style uranium deposits are concentrated in

Jurassic (J), Cretaceous (K), Paleogene (E), and Neogene (N) strata (Fig. 9), followed by the Carboniferous (C) to Triassic (T), and the Quaternary (Q) (Wang et al., 2017a). In South America, uranium ores occur mostly in K and Permian (P), and then in E-N and C-T strata in Argentina, Paraguay, and Brazil (Labenski et al, 1982; Dahlkamp, 2010). In North America, ore-bearing horizons occur mostly in E-N strata in the Wyoming basin and in south Texas (Dahlkamp, 2010), and then in T_3-J_2 strata in the Colorado Plateau (Wang et al., 2017a). In Middle Asia, uranium-bearing strata occur mostly in K_2-E in Kazakhstan and Uzbekistan, and then in T_3-J_1 in East Kyrgyzstan (Dahlkamp, 2010; Wang et al., 2017a). In East Asia, uranium deposits occur mostly in J_2-K strata in China and Russia, and in Mongolia, in K, and then in E_3-N_1 and even in Q strata (Jin et al., 2017; Wang et al., 2017a). In Australia, they occur mostly in K-N strata in the Callabonna sub-Basin, Carnarvon Basin, Gunbarrel Basin and Eucla Basin, and then in C strata in the Canning Basin, Ngalia Basin and Amadeus Basin (Jaireth et al., 2016; Wang et al., 2017a). In Europe, the uranium ore-bearing horizons are older than in other areas, mostly in C-P, and then in E_3-N_1 strata (Dahlkamp et al., 2016; Wang et al., 2017a) as well as in Africa, where they occur in P-T, and also, to a lesser extent, in N strata (Cairncross, 2001; Wang et al., 2017a). From the above, it is obvious that E–N host units are widely distributed in Asia, Eurasia, America, Australia, and Africa (Fig. 9), which indicates that there was widespread uranium mineralization during E–N. Coal–oil data (Jin et al., 2017) reutilized for the sandstone-style uranium deposit survey in China revealed a large number of uranium mineralization in E–N strata (Jin et al., 2017; Zhou et al., 2017). The wide age span of the host units suggests that uranium mineralization might continue to present.

Sandstone uranium mineralization is a hydrogenic and dynamic process, making precise dating very difficult (Ludwig et al., 1982; Placzek et al., 2016; Domnicka et al., 2018). The mineralization age characteristics of the main sandstone-style uranium deposits in the world are assessed (Fig. 10) and all the mineralization ages are listed in Table 1. The statistics suggest that (i) the main stages of mineralization of most sandstone-style uranium deposits occurred from the Miocene to Holocene and the older ages (> 80 Ma) account for approximately less than five percent of these deposits, (ii) uranium mineralization ages exhibited a continuous trend after the Miocene, similar to the "Tanghulu", (iii) most J–K and E–N host units had mineralization ages from the Miocene and Pliocene to the Pleistocene, and (iv) the older ages were residual ores caused by multiple early uplifts and fluid dynamics, and most of them were destroyed by the last tectonic uplift (Fig. 10). The Hangjinqi deposits in the Ordos Basin were used to assess the relationship between the uranium ore that formed from the Miocene to
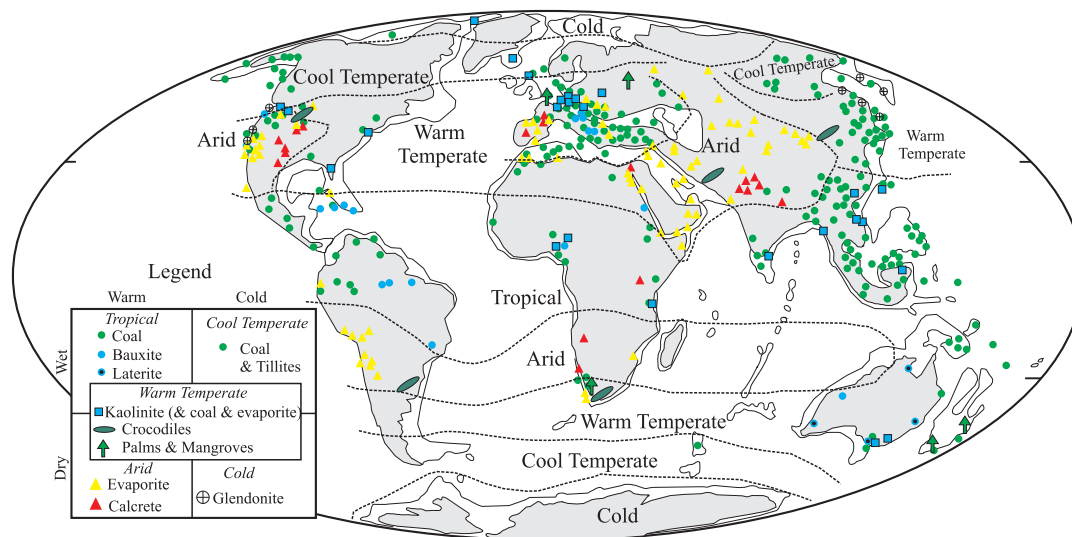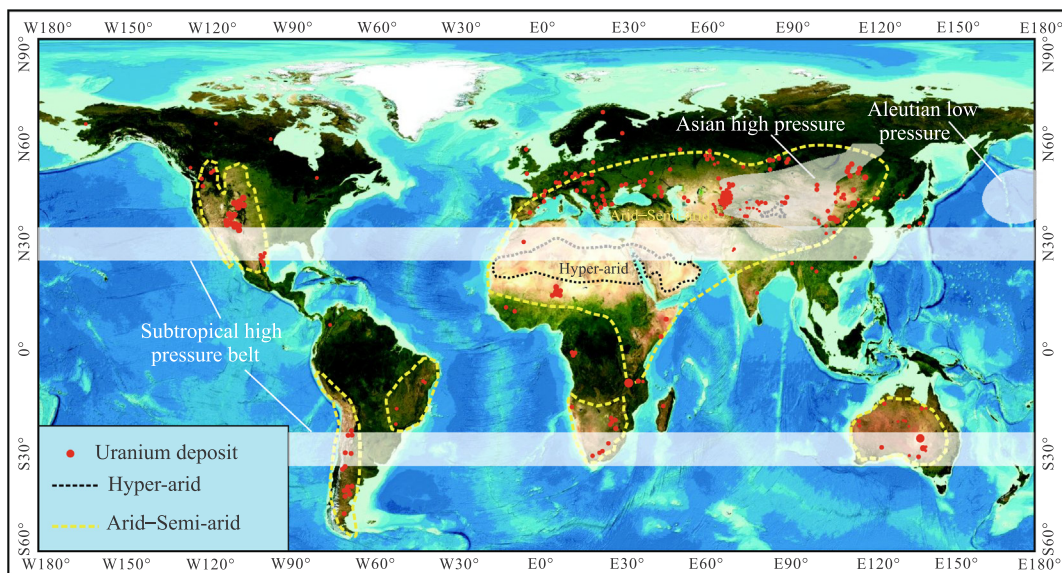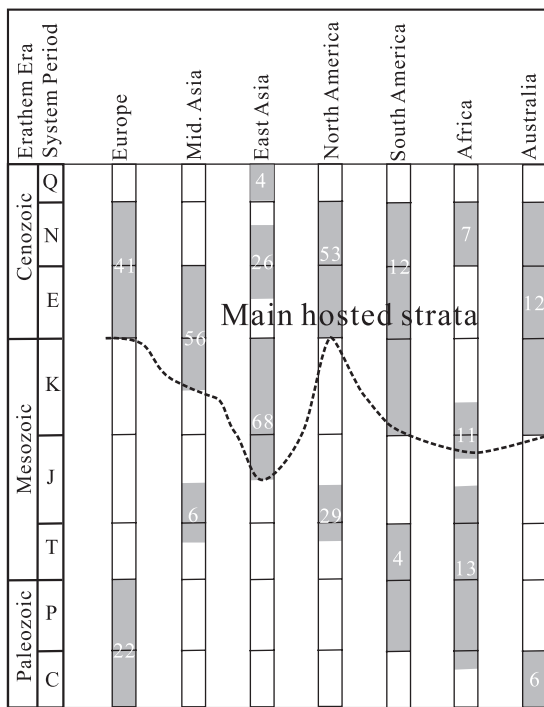

Fig. 7. Climate during the Miocene (from the Paleomap Project, C. R. Scotese, http://www.scotese.com/miocene1.htm).

Fig. 8. Relationship between sandstone-style uranium deposits and modern climate; hyper-arid, arid, and semi-arid distributions are from Qian et al. (2017); uranium deposits are from Fig. 2.
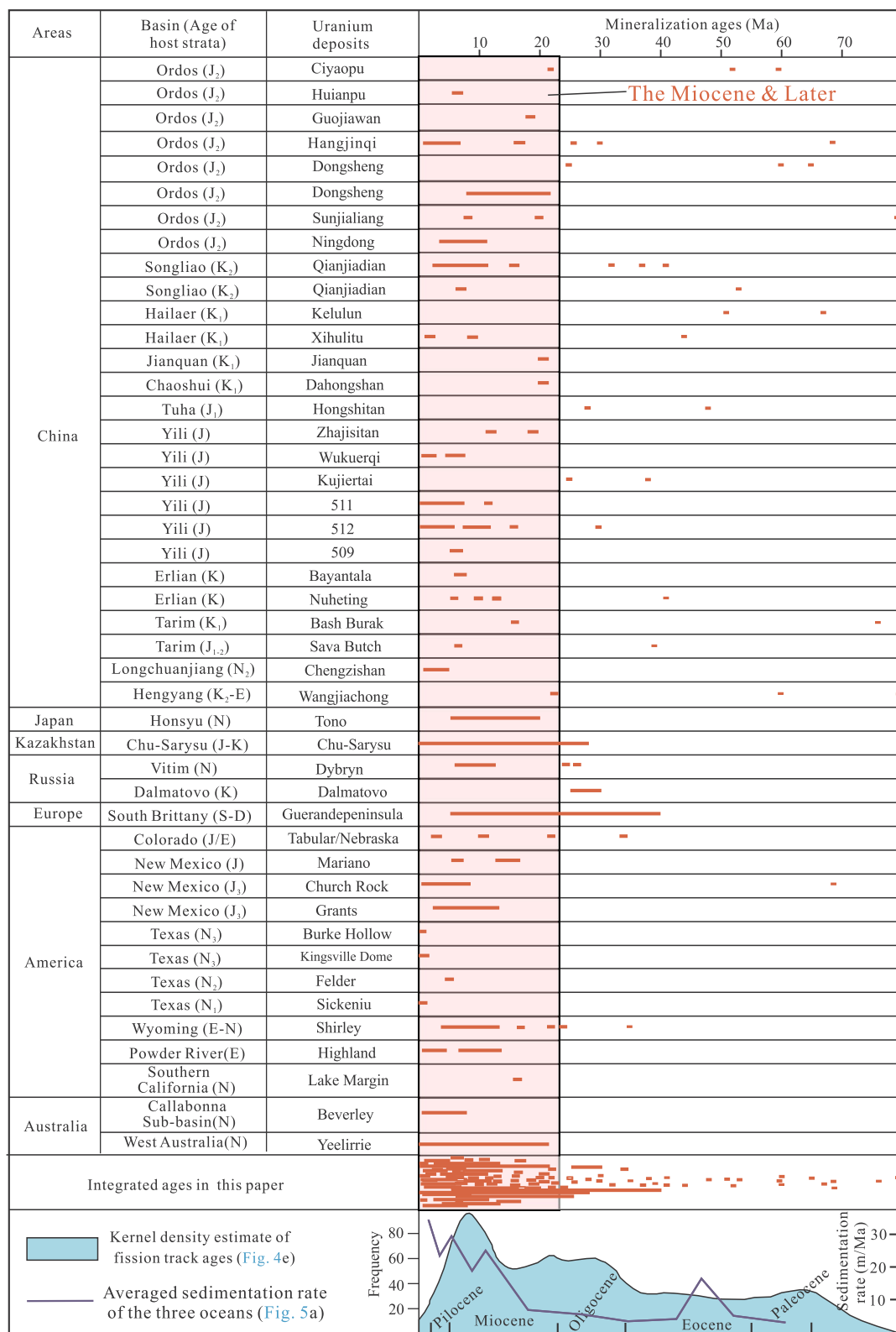

Fig. 9. Host units for sandstone-style uranium deposits in the world (Jin et al., 2016, 2017; Wang et al., 2017a); gray highlights indicate a geologic unit that contains uranium occurrences.

the Holocene, and that which formed prior to the Miocene. Forty-nine in-situ micro U-Pb dating were carried out on coffinite; 32 spots show U-Pb isotope ages of 17.3–1.0 Ma, 11 spots range from 32 to 30 Ma, and 6 spots vary between 69 and 67 Ma. Much of initially formed coffinite was destroyed and the uranium was redistributed in subsequently formed coffinite (Song, 2013; Fig. 11). Ten electron microprobe analyses were conducted on coffinite from the Ningdong deposits in the Ordos Basin, all of which suggest an age range of 10.7–3.9 Ma with no older ages (Wang et al., 2018). In comparison, of 18 electron microprobe analyses conducted on pitchblende from the Qianjiadian deposits in the Songliao Basin, 14 spots fall in the age range of 16.0–3.0 Ma and the rest, vary from 41 to 28 Ma (Zhao et al., 2018). The analytical data

from these three deposits suggest that the formation of sandstone-style uranium deposits occurred between the Miocene and Holocene; few formed in the Paleogene and fewer in the Cretaceous. In general, the overall age distribution trend is characterized by a drastic decrease of older minerals, regardless of deposit (Fig. 10). Other studies revealed a similar phenomenon. Zhao et al. (2013) estimated that regional uranium mineralization in central Asia occurred after 20 Ma. Placzek et al. (2016) proposed that significant uranium leaching and mobility are characteristic of active roll fronts, indicating that uranium mineralization might occur at any time if the appropriate environmental conditions exist. Wang (2002) concluded that sandstone-style uranium deposits mostly formed after the Oligocene, based on a worldwide study of sandstone-style uranium deposits, although recent studies also emphasized Cenozoic mineralization (Chen et al., 2010a; Zhang, 2016; Liu et al., 2017b; Wang et al., 2017a; Zhou et al., 2017). Theoretically, once Earth's atmosphere achieved its present oxygen content, it would have been possible to oxidize exposed uranium minerals to the water-soluble hexavalent form. Therefore, groundwater processes were most likey responsible for the emplacement of epigenetic uranium ores. In fact, uranium mineralization ages from the youngest ores (Fig. 10) suggest that redistributed ores might still be forming today (Ludwig et al, 1982).

5.2. Mineralization and tectonic uplifts

In view of the hydrogenic and dynamic characteristics of sandstone-style uranium deposits, only the relationship between the last regional tectonic uplift and mineralization ages are discussed. There are three main metallogenic belts for sandstone-style uranium deposits that correspond to the tectonic uplifted regions of the Alpine-Himalayan Belt, the Cordillera and the East African Rift, suggesting a close spatiotemporal relationships between sandstone-style uranium deposits and uplift ranges (Fig. 2). For example, the east and west tectonic uplift ages of the Alpine–Himalayan Belt are 20–5 Ma (Fig. 4a) and 14–4 Ma (Fig. 4b) with peaks of 8–10 Ma, which correspond to mineralization ages of 20–0.8 and 40–5 Ma (Fig. 10), respectively. The Cordillera tectonic uplifts occurred at 25–4 Ma (Fig. 4d), with peaks at 5–7 Ma (Kay and Kay, 2002), and the mineralization ages are mostly at 17–0.1 Ma (Fig. 10). The central range epeirogenic uplift in Australia occurred at ~ 12 Ma (Van Ufford and Cloos, 2005) and the mineralization ages are mostly at 6.7–0.4 Ma (Wülser et al., 2011). The

Fig. 10. Global sandstone-style uranium mineralization ages, most of which occur in the Miocene and later, corresponding to the intense Miocene tectonic uplift; the uranium deposit ages are from Dooley et al. (1974), Ludwig et al. (1982), Rosenberg and Hooper (1982), Cathelineau and Holliger (1988), Cole et al. (2001), Xia et al. (2003, 2004, 2015), Xiao et al. (2003), Liu et al. (2004), Zhang et al. (2005), Cai et al., (2007); Liu et al. (2009b), Chen et al. (2010b), Wülser et al. (2011), Golubev et al. (2013), Song (2013), Meek (2014), Zhu et al. (2014), Jaireth et al. (2016), Hall et al. (2017), Wang et al. (2018), Zhao et al. (2018) and Zhang et al. (2018).

Table 1
Ages of mineralization of typical sandstone-style uranium deposits in the world.

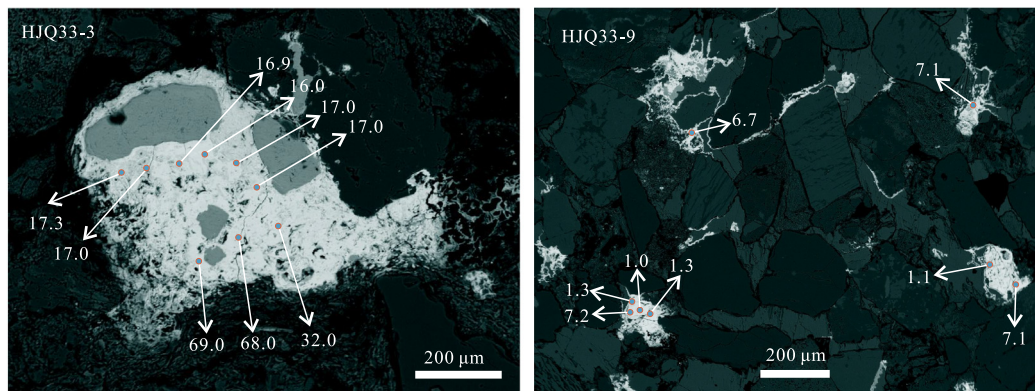| Continental tilts	Uplift fission track ages	Basin	Uranium deposits	Mineralization age (Ma)	Analysis method	Age of host strata	Reference
Alps-Himalaya	20–5 Ma	Ordos	Hangjinqi	68.6, 30.0, 16.9, 7.07, 1.2	Uraninite U-Pb	J2	Song, 2013
		Ordos	Daying	91, 37, 17.5	Uraninite U-Pb	J2	Song, 2013
		Ordos	Nalinggou	30.0, 25.1, 16.7, 7.07, 3.46, 1.2	Uraninite U-Pb	J2	Wu et al., 2015
		Ordos	Ciyaopu	59.6, 52.0, 21.9	Coffinite U-Pb	J2	Chen et al., 2010b
		Ordos	Huianpu	6.8, 6.2	whole rock U-Pb	J2	Chen et al., 2010b
		Ordos	Guojiawan	98.0, 18.6	whole rock U-Pb	K1	Chen et al., 2010b
		Ordos	Dongsheng1	65–60, 25.0	U-Pb	J2	Zhang et al., 2018
		Ordos	Dongsheng2	22~9.8	Coffinite U-Pb	J2	Cai et al., 2007
		Ordos	Sunjialiang	186, 177, 120, 80.0, 20.0, 8.0	whole rock U-Pb	J2	Xia, 2015
		Ordos	Ningdong	10.7, 9.6, 9.0, 8.5, 6.6, 6.6, 5.1, 4.7, 4.2, 3.9	Coffinite EPMA	J2	Wang et al., 2018
		Songliao	Qianjiadian	41.0, 37.0, 32.0, 16.0, 11.0, 10.0, 8.0, 6.0, 6.0, 5.0, 5.0, 5.0, 4.0, 4.0, 3.0, 3.0, 3.0	Coffinite EPMA	K2	Zhao et al., 2018
		Songliao	Qianjiadian, Baixingtu	96, 67, 53.0, 52, 40, 7.0	whole rock U-Pb	K2	Zhang et al., 2005
		Hailaer	Kelulun	67.0, 51.0	whole rock U-Pb	K1	Xia et al., 2004
		Hailaer	Xihulitu	81.0, 44.0, 9.0, 2.0	whole rock U-Pb	K1	Xia et al., 2004
		Jiudong	honggouyao	106.0, 57.0	whole rock U-Pb	K1	Chen et al., 2010b
		Jianquan	Jianquan	113.0, 21.4	whole rock U-Pb	K1	Chen et al., 2010b
		Chaoshui	Dahongshan	21.4	whole rock U-Pb	K1	Chen et al., 2010b
		Tuha	Hongshitan	48.0, 28.0	whole rock U-Pb	J1	Liu et al., 2004
		Yili	Kujieertai, Zhajisitan	38.0, 25.0, 19.0, 12.0	whole rock U-Pb	J	Chen et al., 2010b
		Yili	Wukuerqi	7.0, 5.0, 2.0, 1.0	whole rock U-Pb	J	Chen et al., 2010b
		Yili	Kujiertai	38.0, 25.0	whole rock U-Pb	J	Chen et al., 2010b
		Yili	511	11.4, 6.9, 6.1, 5.4, 3.2, 2.7, 2.7, 1.9, 0.7	whole rock U-Pb	J	Xia et al., 2003
		Yili	512	29.8, 15.9, 11.5, 11.1, 10.2, 8.0, 8.0, 8.1, 5.3, 4.6, 4.1, 3.5, 3.1, 2.0, 1.7, 1.2, 0.8	whole rock U-Pb	J	Xia et al., 2003
		Yili	509	6.7, 5.7	whole rock U-Pb	J	Xia et al., 2003
		Erlian	Bayantala	7	whole rock U-Pb	K	Xia et al., 2003
		Erlian	Nuheting	85.0, 41.0, 13.0, 10.0, 6.0	whole rock U-Pb	K2	Chen et al., 2010b
		Tarim	Bash Burak	76.0, 16.0	whole rock U-Pb	K1	Chen et al., 2010b
		Tarim	Sava Butch	38.9, 6.6	whole rock U-Pb	J1-2	Liu et al., 2009b
		Longchuanjiang	Chengzishan	4.4, 43.6, 2.2	whole rock U-Pb	N2	Chen et al., 2010b
		Hengyang	Wangjiachong	80.0, 60.0, 22.5	whole rock U-Pb	K2-E	Chen et al., 2010b
		Honsyu	Tono	20–5	Coffinite U-Pb	N	Komuro, 2009
		Chu-Sarysu	Chu-Sarysu	Late Oligocene to Quaternary	U-Pb	J-K	Jaireth et al., 2016
		Vitim	Dybryn	26.9, 23.2, 12.5, 12.0, 10.2, 9.5, 9.3, 8.6, 7.4, 6.5	Uraninite U-Pb	N	golubev et al., 2013
		Dalmatovo	Dalmatovo	30~25	whole rock U-Pb	K	Xiao et al., 2003
		South Brittany	Guerande Peninsula	40~5	U-Pb	S-D	Cathelineau and Holliger, 1988
Cordillera-Andes	25–4 Ma	Colorado	Tabular/Nebraska	34, 22, 11, 3	Uranium U-Pb	J/E	Meek, 2014
		New Mexico	Mariano	15.9, 13.8, 6.7, 6.6	Fission Track	J	Rosenberg and Hooper, 1982
		New Mexico	Church Rock	68.7, 7.8, 1.1, 1.1, 1.0, 0.97, 0.91, 0.83, 0.62, 0.49, 0.49, 0.49, 0.49, 0.47, 0.11	whole rock U-Pb	J3	Ludwig et al., 1982
		New Mexico	Grants	12.5~3.3	Coffinite EMPA	J3	Jaireth et al., 2016
		New Mexico	Grants	36.6~0.7	Coffinite EMPA	J3	Deditius et al., 2008
		Texas	Burke Hollow	very young	U-Pb	N3	Hall et al., 2017
		Texas	Kingsville Dome	0.45~0.15	U-Pb	N3	Hall et al., 2017
		Texas	Felder	5.07	U-Pb	N2	Hall et al., 2017
		Texas	Sickeniu	< 0.25	U-Pb	N1	Hall et al., 2017
		Wyoming	Shirley	35, 24, 22, 17, 13~4.5	whole rock U-Pb	E-N	Dooley et al., 1974; Santos and Ludwig, 1983
Australian	central about 12 Ma; southeastern 50–25 Ma	Powder River	Highland	13~7, 4.3, 1.7, 1.7, 1.6, 1.2, 1.1, 1.0, 0.91	whole rock U-Pb	E	Ludwig et al., 1982
		Southern California	Lake Margin	16.4	U-Pb	N	Cole et al., 2001
		Callabonna Sub-basin	Beverley	6.7~0.4, 5.5~3.4	Coffinite U-Pb	N	Wülser et al., 2011
		West Australia	Yeelirrie	Neogene-Quaternary	Stratum	N	Zhu et al., 2014

Fig. 11. Laser ablation back-scattered images and U-Pb isotope age (Ma) distribution of the Hangjinqi uranium ore deposit in the Ordos Basin (Song, 2013); white highlights indicate coffinite; the ages indicate that most of the coffinites formed during the Miocene or later; very few residual coffinites were identified; images courtesy Professor B. L. Wu, Northwestern University.

eastern Ordos Basin was uplifted at 20–8 Ma; mineralization ages close to the uplift range were estimated at 17.3–1.0 Ma for the Hangjinqi deposits (Song, 2013) and at 10.7–3.9 Ma (Wang et al., 2018). The Qianjiadian uplifted at 38–10 Ma with peak uplift occurring at ~16 Ma (Cheng et al., 2018), while the mineralization ages broadly cluster at 41–3 Ma with peaks at 16–3 Ma. The tectonic uplift of these three mountain ranges resulted in continental tilts along their length that provided good tectonic conditions for fluid migration and the formation of sandstone-style uranium deposits. Their last rapid uplift ages were from the Middle and Late Miocene (Fig. 4e).

Recent studies discuss how tectonic uplift may have controlled uranium mineralization. For example, Jin et al. (2016) identified intra-basin uplift-related uranium mineralization with coal–oil data re-utilized for a sandstone-style uranium deposit survey in China, and emphasized the types of structures controlling the migration of fluids in the mineralization process. Liu et al. (2017a,b) suggested that an orogenic hydrothermal solution derived from strong folding and the orogeny of Tianshan has, since the Miocene, reformed former uranium ore bodies. Cheng et al. (2018) proposed that the tectonic inversion from the Oligocene to the Miocene controlled the regional uranium mineralization in the Songliao Basin. Hou (2010) indicated that the 40–26 Ma tectonic inversion caused fluid activity in the vicinity of the Himalaya, forming regional uranium deposits on continental tilts over thousands of kilometers (Jin et al., 2017). Saucier (1980) suggested that the Zuni uplift, formed during the Tertiary in New Mexico, USA controlled the oxidative destruction and redistribution of primary uranium ore deposits into redistributed or stacked ore, and controlled the regional incursion of oxidizing groundwater well into the basin. In Australia, the last Miocene uplift events with ages of 6–4 Ma at Lake Frome resulted in the formation of the Beverley ore deposit at 6.7 to 0.4 Ma, redistributing prior uranium ore deposits (Wülser et al., 2011; Jaireth et al., 2016). In other words, sandstone-style uranium deposits are the result of the last regional tectonic uplift that controlled fluid migration, erosion, sedimentation, and mineralization.

5.3. Mineralization and climate

Based on the hydrogenic and dynamic characteristics of sandstone uranium mineralization, the regional climate influences groundwater, playing an important role in the uranium mineralization process. The distribution of sandstone-style uranium deposits and modern climate (Fig. 8) indicate that sandstone-style uranium deposits were mainly distributed in arid and semi-arid areas, which are mainly controlled by SHPBs characterized by drought and less rain on both sides of the equator, till ~30° latitude. The sandstone-style uranium deposit distribution of the Alpine–Himalayan mineralization belt is mainly north of the SHPB and the Asian high-pressure region (Fig. 8) in the northern

hemisphere. The distribution of sandstone-style uranium deposits of the Cordillera and East African Rift mineralization belts are near the crossing of ranges and SHPBs (Fig. 2). Hyper-arid areas are not suitable for uranium mineralization because of the lack of sufficient fluid supply, such as in northern Africa. Similarly, humid areas are also not suitable for uranium mineralization because excess groundwater might redistribute prior uranium ores (Ludwig et al., 1982), which is not conducive to their preservation, as seen in southeast China. An Asian high-pressure region might influence arid regions with less rain, such as in northwest China, Kazakhstan, Mongolia, and south Russia, all of which are favored uranium metallogenic areas.

During the Miocene, especially in the Middle and Late Miocene, global plate activity was very intense and formed regional magma belts, folding and faulting belts, and tectonic uplift along the Alpine–Himalayan Belt, the circum-Pacific orogenic belt and the East Africa Rift belt. These tectonic events reshaped the global landscape and formed many of today's major river systems (Harrison et al., 1992; Gradstein et al., 2004; Clark and Bilham, 2008; Potter and Szatmari, 2009, 2015; Bracciali et al., 2015; Wang, 2017b). Regional continental tilts formed along these ranges enabling uranium-rich fluid migration and mineralization, forming sandstone-style uranium deposits. These intense tectonic events of the Miocene formed modern geomorphology and influenced climate (Gradstein et al., 2004; Potter and Szatmari, 2009, 2015; Xiao et al., 2014). Uranium mineralization was controlled by local groundwater conditions, which might have redistributed prior ores if oxidation conditions persisted (Ludwig et al., 1982; Xia, 2015; Jin et al., 2016; Placzek et al. 2016). Consequently, sandstone-style uranium deposits may still be forming today, under reducing conditions. Arid and semi-arid areas are favorable regions for sandstone-style uranium deposits because less rain is beneficial to ore preservation, while oxygenated water redistributes prior ores.

Global tectonic events in the Miocene caused the uplift of three regional mountain ranges, the Alpine–Himalayan Belt, the Cordillera, and the East African Rift, along with continental tilts which controlled the migration of groundwater and influenced local climate. Modern climate had almost formed in the Miocene with the SHPBs on both sides of the equator, extending to around 30° latitude, influencing rainfall patterns. All these factors controlled the mineralization and distribution of sandstone-style uranium deposits (Fig. 12). In the first-stage of the formation of uranium ores, percolating rainwater carried ^{+6}U to prior strata, consuming the reducing medium. During the second-stage, rainwater again carried ^{+6}U to prior strata, consuming the next reducing medium, and forming second-stage uranium ores, and so on; later stage uranium ores may have formed on complete or partial destruction of prior stage ores if the percolating groundwater carried enough oxygen. The previously formed ores were mostly destroyed by the latest tectonic uplift and oxygenic fluids, preserving a little residual ore and
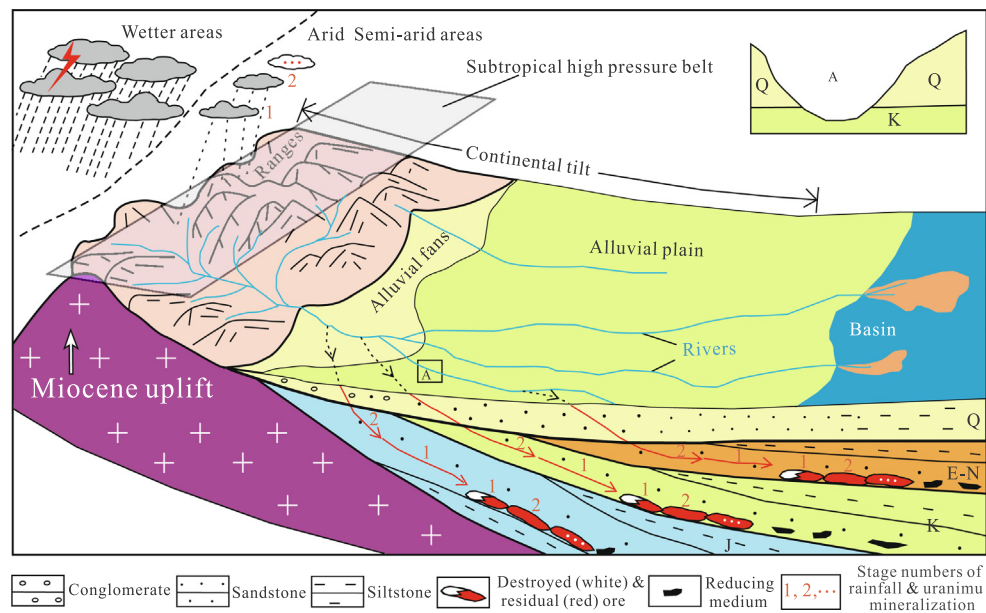
Fig. 12. Miocene uplift ranges and rainfall patterns facilitating sandstone-style uranium mineralization; J: Jurassic; K: Cretaceous; E-N: Paleogene–Neogene; Q: Quaternary.

forming new ores. The last tectonic uplift in the Miocene was the most dynamic factor in this mineralization; subsequently, multiple uranium ores may have formed because of interaction with oxygenic fluids (Fig. 12).

6. Conclusions

Intense global tectonic events in the Middle and Late Miocene have shaped modern geomorphology, resulting in the regional uplift of ranges and continental tilts that developed along the Alpine–Himalayan Belt, the Cordillera, and the East African Rift, among others.

These ranges and continental tilts controlled the migration directions of uranium-bearing fluids which, in turn, controlled the formation and distribution of sandstone-style uranium deposits, most of which have spatiotemporal characteristics related to Miocene tectonics around the world.

Regional uplift of the Alpine–Himalayan Belt, the Cordillera, and the East African Rift occurred between 20 and 5 Ma; uranium mineralization ages are estimated to have occurred during 20–0.1 Ma, with evidence for multiple remobilizations; some of these remobilizations continued through the Holocene.

Modern-day climate had almost fully formed during the Miocene, and the development of the SHPBs on both sides of the equator along with the Asian high-pressure region controlled the occurrence of arid and semi-arid areas, as well as rainfall patterns, influencing the distribution of sandstone-style uranium deposits.

References

Armijo, R., Lacassin, R., Curveur, A.C., Carrizob, D., 2015. Coupled tectonic evolution of Andean orogeny and global climate. Earth Sci. Rev. 143, 1–35.

Balestrieri, M.L., Bonini, M., Corti, G., Sani, F., Philippon, M., 2016. A refinement of the chronology of rift-related faulting in the Broadly Rifted Zone, southern Ethiopia, through apatite fission-track analysis. Tectonophysics 671, 42–55.

Balestrieri, M.L., Benvenuti, M., Tangocci, F., 2013. Detrital fission-track-compositional signature of an orogenic chain-hinterland basin system: the case of the late Neogene Quaternary Valdelsa basin (Northern Apennines, Italy). Sed. Geol. 289, 159–168.

Balestrieri, M.L., Ferrari, L., Bonini, M., Duque-Trujillo, D., Cerca, M., Moratti, G., Corti, G., 2017. Onshore and offshore apatite fission-track dating from the southern Gulf of California: insights into the time-space evolution of the rifting. Tectonophysics 719–720, 148–161.

Balestrieri, M.L., Stuart, F.M., Persano, C., Abbate, E., Bigazzi, G., 2005. Geomorphic development of the escarpment of the eritrean margin, southern red sea from combined apatite fission-track and (u–th)/he thermochronometry. Earth Planet. Sci. Lett. 231, 97–110.

Barbarand, J., Lucazeau, F., Pagel, M., Seranne, M., 2001. Burial and exhumation history of the south-eastern Massif Central (France) constrained by apatite fission-track thermochronology. Tectonophysics 335, 275–290.

Bojara, A.V., Neubauerb, F., Fritza, H., 1998. Cretaceous to Cenozoic thermal evolution of the southwestern South Carpathians: evidence from fission-track thermochronology. Tectonophysics 297, 229–249.

Boulton, S.J., Smart, C.W., Consolaro, C., Snider, A., 2016. The Miocene-Pliocene boundary and the Messinian Salinity Crisis in the easternmost Mediterranean: insights from the Hatay Graben (Southern Turkey). Sediment Geol. 332, 51–67.

Bracciali, L., Najman, Y., Parrish, R.R., Akhter, S.H., Millar, I., 2015. The Brahmaputra tale of tectonics and erosion: Early Miocene river capture in the Eastern Himalaya. Earth Planet. Sci. Lett. 415, 25–37.

Brown, R., Summerfield, M., Gleadow, A., Gallagher, K., Carter, A., Beucher, R., Wildman, M., 2014. Intracontinental deformation in southern Africa during the Late Cretaceous. J. Afr. Earth Sc. 100, 20–41.

Cairncross, B., 2001. An overview of the Permian (Karoo) coal deposits of southern Africa. J. Afr. Earth Sc. 33, 529–562.

Cai, C.F., Dong, H.L., Li, H.T., Xiao, X.J., Ou, G.X., Zhang, C.M., 2007. Mineralogical and geochemical evidence for coupled bacterial uranium mineralization and hydrocarbon oxidation in the Shashagetai deposit, NW China. Chem. Geol. 236, 167–179.

Carmo, I.D.O., Vasconcelos, P., 2004. Geochronological evidence of pervasive Miocene weathering, Minas Gerais, Brazil. Earth Surf. Process. Landf 29, 1303–1320.

Cathelineau, M., Holliger, P., 1988. Uranium mineralizations in western Europe: the witness of major geodynamic events from devonian to tertiary. Chem. Geol. 70 188 188.

Cuney, M., 2013. Uranium and thorium resources and sustainability of nuclear energy. Uranium: Cradle to Grave, MAC Short Course Series 43 (15), 417–438.

Chen, Z.L., Lu, K.G., Wang, G., Chen, B.L., Wang, G.R., Zheng, E.J., Cui, L.L., Ding, W.J., 2010a. Characteristics of Cenozoic structural movements in southern margin of Junggar basin and its' relationship to the mineralization of sandstone-type uranium deposits. Acta Petrologica Sinica 26, 457–470 (in Chinese with English abstract).

Chen, Z.Y., Chen, D.S., Gu, K.H., Wang, Y.J., 2010b. The regional distribution regularities of ore-hosting horizon, deposit type and mineralization age of China's sandstone-hosted uranium deposits. Uranium Geol. 26, 321–330 (in Chinese with English

abstract).

Cheng, Y., Wu, Z., Yan, S., Xu, C., Li, W., Zhang, J., Zhang, S., Ren, J., Su, W., Zhang, J., 2015. Cenozoic tectonic evolution of Liaodong dome, Northeast Liaodong Bay, Bohai, offshore China, constraints from seismic stratigraphy, vitrinite reflectance and apatite fission track data. Tectonophysics 659, 152–165.

Cheng, Y.H., Wang, S.Y., Li, Y., Ao, C., Li, Y.F., Li, J.G., Li, H.L., Zhang, T.F., 2018. Late Cretaceous-Cenozoic thermochronology in the southern Songliao Basin, NE China: New insights from apatite and zircon fission track analysis. J. Asian Earth Sci. 160, 95–106.

Clark, M.K., Bilham, R., 2008. Miocene rise of the Shillong Plateau and the beginning of the end for the Eastern Himalaya. Earth Planet. Sci. Lett. 269, 337–351.

Cole, J.M., Rasbury, E.T., Montañez, I.P., Pedone, V.A., Hemming, S.R., Lanzirotti, A., Becker, M.L., Hanson, G.N., 2001. Uranium-Lead ages of Lake Margin Tufa calcite from the Middle Miocene Barstow Formation, Southern California. Agu Fall Meeting Abstracts id. V42F–04.

Coltice, N., Gérault, M., Ulvrová, M., 2017. A mantle convection prespective on global tectonics. Earth Sci. Rev. 165, 120–150.

Compton, J.S., Mallinson, D.F., 1996. Geochemical consequences of increased late Cenozoic weathering rates and the global CO_2 balance since 100 Ma. Paleoceanography 11, 431–446.

Dahlkamp, F.J., 2010. Uranium Deposits of the World: USA and Latin America. Springer-Verlag, Berlin Heidelberg, pp. 1–535.

Dahlkamp, F.J., 2016. Uranium Deposits of the World: Europe. Springer-Verlag, Berlin Heidelberg, pp. 1–792.

Deditius, A.P., Utsunomiya, S., Ewing, R.C., 2008. The chemical stability of coffinite, $USiO_4 \cdot nH_2O$; $0 < n < 2$, associated with organic matter: a case study from Grants uranium region, New Mexico, USA. Chem. Geol. 251, 33–49.

Domnicka, U., Cook, N.J., Bluckb, R., Brown, C., Ciobanu, C.L., 2018. Petrography and geochemistry of granitoids from the Samphire Pluton, South Australia: implications for uranium mineralization in overlying sediments. Lithos 300–301, 1–19.

Dooley, J.R., Harshman, E.N., Rosholt, J.N., 1974. Uranium-Lead ages of the uranium deposits of the Gas Hills and Shirley Basin, Wyoming. Econ. Geol. 69, 527–531.

Dooley, T.P., Jackson, M.P.A., Hudec, M.R., 2013. Coeval extension and shortening above and below salt canopies on an uplifted, continental margin: application to the northern Gulf of Mexico. Am. Assoc. Pet. Geol. Bull. 917, 1737–1764.

Enkelmann, E., Piestrzeniewicz, A., Falkowski, S., Stübner, K., Ehlers, T.A., 2017. Thermochronology in southeast Alaska and southwest Yukon: Implications for North American Plate response to terrane accretion. Earth Planet. Sci. Lett. 457, 348–358.

Esteban, J.J., Tubía, J.M., Cuevas, J., Seward, D., Larionov, A., Sergeev, S., Navarro-Vilá, F., 2013. Insights into extensional events in the Betic Cordilleras, southern Spain: New fission-track and U-Pb SHRIMP analyses. Tectonophysics 603, 179–188.

Eyles, C.H., Eyles, N., Lagoe, M.B., 1991. The Yakataga formation; a Late Miocene to Pleistocene record of temperate glacial marine sedimentation in the Gulf of Alaska. In: Anderson, J.B., Ashley, G.M. (Eds.), Glacial Marine Sedimentation, Paleoclimatic Significance. Geol. Society Am. Spec. Paper 261, 159–180.

Eyles, N., 1996. Passive margin uplift around the North Atlantic region and its role in Northern Hemisphere late Cenozoic glaciation. Geology 24, 103–106.

Faccenna, C., Bellier, O., Martinod, J., Piromallo, C., Regard, V., 2006. Slab detachment beneath eastern Anatolia: a possible cause for the formation of the North Anatolian fault. Earth Planet Sci. Lett. 242, 85–97.

Farley, K.A., Rusmore, M.E., Bogue, S.W., 2001. Post 10 ma uplift and exhumation of northern coastal mountains, British Columbia. Geology 29, 99–102.

Foster, D.A., Gleadow, A.J.W., 1992. The morphotectonic evolution of rift-margin mountains in central Kenya: constraints from apatite fission-track thermochronology. Earth Planet. Sci. Lett. 113, 157–171.

Garzione, C.N., Hoke, G.D., Libarkin, J.C., Withers, S., Macfadden, B., Eiler, J., Ghosh, P., Muich, A., 2008. Rise of the Andes. Science 320, 1304–1307.

Gleadow, A.J.W., Kohn, B.P., Brown, R.W., O'Sullivan, P.B., Raza, A., 2002. Fission track thermotectonic imaging of the Australian continent. Tectonophysics 349, 5–21.

Golubev, V.N., Chernyshev, I.V., Chugaev, A.V., Eremina, A.V., Baranova, A.N., Krupskaya, V.V., 2013. U-Pb systems and U isotopic composition of the sandstone-hosted paleovalley Dybryn uranium deposit, Vitim uranium district, Russia. Geol. Ore Deposits 55, 399–410.

Gradstein, F.M., Ogg, J.G., Smith, A.G. (Eds.), 2004. A geologic time scale 2004. Cambridge University, Cambridge, pp. 589.

Guillocheau, F., Simon, B., Baby, G., Bessin, P., Robina, C., Dauteuil, O., 2018. Planation surfaces as a record of mantle dynamics: the case example of Africa. Gondwana Res. 53, 82–98.

Guo, Z.T., Ruddiman, W.R., Hao, Q.Z., Wu, H.B., Qiao, Y.S., Zhu, R.X., Peng, S.Z., Wei, J.J., Yuan, B.Y., Liu, T.S., 2002. Onset of Asian desertification by 22 Myr ago inferred from Loess deposits in China. Nature 416, 159–163.

Hall, S.M., Mihalasky, M.J., Tureck, K.R., Hammarstrom, J.M., Hannon, M.T., 2017. Genetic and grade and tonnage models for sandstone-hosted roll-type uranium deposits, Texas Coastal Plain, USA. Ore Geol. Rev. 80, 716–753.

Harrison, T.M., Copeland, P., Kidd, W., Yin, A., 1992. Raising Tibet. Science 155 (1663–1), 670.

Hilgren, F.J., Lourens, L.J., Van Dam, J.A., 2012. The neogene period. In: Gradstein, F.M., Ogg, J.G., Schmitz, M.D., Ogg, G.M. (Eds.), The Geologic Time Scale. Elsevier Boston, pp. 32–978.

Hoorn, C., Wesselingh, F.P., ter Steege, H., Bermúdez, M.A., Mora, A., Sevink, J., Sanmartín, I., Sanchez-Meseguer, A., Anderson, C.L., Figueiredo, J.P., Jaramillo, C., Riff, D., Negri, F.R., Hooghiemstra, H., Lundberg, J., Stadler, T., S€arkinen, T., Antonelli, A., 2010. Amazonia through time: andean uplift, climate change, landscape evolution and biodiversity. Science 330, 927–931.

Hou, Z.Q., 2010. Metallogensis of continental collision. Acta Geol. Sin. 84, 30–58 (in Chinese with English abstract).

Hsü, K.J., 1983. The Mediterranean was a Desert. Princeton University Press, Princeton, pp. 197.

Hsü, K.J., Montadert, L., Bernoulli, D., Cita, M.B., Erickson, A., Garrison, R.E., 1977. History of the Mediterranean salinity crisis. Nature 267, 399–403.

Issawi, B., Mccauley, J.F., 1993. The Cenozoic landscape of Egypt and its river systems. Ann. Geol. Survey Egypt XIX 357–384.

Jaireth, S., Roach, I.C., Bastrakov, E., Liu, S.F., 2016. Basin-related uranium mineral systems in Australia: a review of critical features. Ore Geol. Rev. 76, 360–394.

Jelinek Jr, A.R.F.C., Beek, P.A.V.D., Guadagnin, F., Cupertino, J.A., Viana, A., 2014. Denudation history and landscape evolution of the northern East-Brazilian continental margin from apatite fission-track thermochronology. J. S. Am. Earth Sci. 54, 158–181.

Jiao, Y.Q., Wu, L.Q., Peng, Y.B., Rong, H., Ji, D.M., Miao, A.S., Li, H.L., 2015. Sedimentary-tectonic setting of the deposition-type uranium deposits forming in the Paleo-Asian tectonic domain, North China. Earth Sci. Front. 22, 189–205 (in Chinese with English abstract).

Jin, R.S., Cheng, Y.H., Li, J.G., Sima, X.Z., Miao, P.S., Wang, S.Y., Ao, C., Li, H.L., Li, Y.F., Zhang, T.F., 2017. Late Mesozoic continental basin "red and black" coupling for sandstone uranium mineralization in northern China. Geol. China 44, 205–223 (in Chinese with English abstract).

Jin, R.S., Miao, P.S., SiMa, X.Z., Li, J.G., Zhao, H.L., Zhao, F.Q., Feng, X.X., Chen, Y., Chen, L.L., Zhao, L.J., Zhu, Q., 2016. Structure styles of Mesozoic-Cenozoic U-bearing rock series in Northern China. Acta Geologica Sinica (English Edition) 90, 2104–2116.

Juez-Larré, J., Andriessen, P.A.M., 2002. Post Late Paleozoic tectonism in the southern Catalan Coastal Ranges (NE Spain), assessed by apatite fission track analysis. Tectonophysics 349, 113–129.

Karaoğlan, F., Parlak, O., Hejl, E., Neubauer, F., Klötzli, U., 2016. The temporal evolution of the active margin along the Southeast Anatolian Orogenic Belt (SE Turkey): evidence from U-Pb, Ar–Ar and fission track chronology. Gondwana Res. 33, 190–208.

Kay, R.W., Kay, S.M., 2002. Andean adakites: Three ways to make them. Acta Petrol Sin 18, 303–311.

Keller, G., Barron, J.A., 1983. Paleogeographic implications of Miocene deep-sea hiatuses. Geol. Soc. Am. Bull. 94, 590–613.

Kominz, M.A., 1984. Oceanic ridge volumes and sea level changedan error analysis. In: Schlee, J.S. (Ed.), Interregional Unconformities and Hydrocarbon Accumulations, Am. Assoc. Pet. Geol. Memoir 36, 109–127.

Kosei Komuro K., Yaguchi M., Sasao E., 2009. Lead isotopes of the Tono uranium deposits: uranium ore formation and radionuclides migration. http://www.geol.tsukuba.ac.jp/EarthResource/index.html.

Krijsman, W., Hilgen, F.J., Raff, I., Sierro, F.J., Wilson, D.S., 1999. Chronology, causes, and progression of the Messinian salinity crises. Nature 400, 652–655.

Labenski, F., Saragovi-Badler, C., Nicolli, H.B., 1982. Genesis of sandstone-type uranium deposits in the Sierra Pintada district, Mendoza, Argentina: a Moessbauer study. Uranium 1, 1–17.

Langford, R.P., Wilford, G.E., Truswell, E.M., Isern, A.R., 1995. Paleogeographic Atlas of Australia, vol. 10, 37.

Li, G.J., Pettke, T., Chen, J., 2011. Increasing Nd isotopic ratio of Asian dust indicates progressive uplift of the north Tibetan plateau since the Middle Miocene. Geology 39, 199–202.

Li, J.H., Yang, J.Y., Cheng, Y.L., Li, W.B., Zhou, X.B., 2013. Structure and evolution characteristics of the global sedimentary basins: Evidence from the N-S long profiles. Geol. J. China Univ. 19, 561–573 (in Chinese with English abstract).

Lin, X., Zheng, D., Sun, J., Windley, B.F., Tian, Z., Gong, Z., Jia, Y., 2015. Detrital apatite fission track evidence for provenance change in the Subei Basin and implications for the tectonic uplift of the Danghe Nan Shan (NW China) since the mid-Miocene. J. Asian Earth Sci. 111, 302–311.

Liu, C.Y., Qiu, X.W., Wu, B.L., Zhao, H.G., 2009a. Subdivisions of the Central-East Asia multi-energy minerals metallogenetic domain and types of those basins. Xinjiang Petroleum Geol. 30, 412–418 (in Chinese with English abstract).

Liu, H.X., Dong, W.M., Liu, Z.Y., Chen, X.L., 2009b. Mesozoic-Cenozoic tectonic evolution and its relation to sandstone-type uranium mineralization in northern Tarim area: Evidence from apatite fission track. World Nuclear Geosci. 26, 125–133 (in Chinese with English abstract).

Liu, H.B., Xia, Y.L., Lin, J.R., Fan, G., 2004. Isotope geology of the sandstone type uranium deposit in Turpan-Hami Basin. Acta Geoscientica Sinica 25, 196–198 (in Chinese with English abstract).

Liu, X.Y., Zhang, Q., Zhang, C.L., Yuan, F.L., Jiao, S.T., 2017a. Global major events in Miocene and its significance: revelation from data mining (in Chinese). Chin Sci. Bull. 62, 1645–1654 (in Chinese with English abstract).

Liu, Z.Y., Peng, S.P., Qin, Mingkuan, Liu, H.X., Huang, S.H., He, Z.B., Guo, Q., Xu, Q., Song, J.Y., 2017b. Multistage enrichment of the Sawafuqi Uranium Deposit: New insights into sandstone-hosted uranium deposits in the intramontane basins of Tian Shan, China. Acta Geol. Sin. 91, 2138–2152.

Lu, H.Y., Guo, Z.T., 2013. Evolution of the monsoon and dry climate in East Asia during late Cenozoic: a review. Sci. China Earth Sci. 57, 70–79 (in Chinese with an English abstract).

Ludwig, K.R., Rubin, B., Fishman, N.S., Reynolds, R.L., 1982. U-Pb ages of uranium ores in the Church Rock uranium district, New Mexico. Econ. Geol. 77, 1942–1945.

Lugli, S., Manzi, V., Roveri, M., Schreiberc, B.C., 2015. The deep record of the Messinian salinity crisis: evidence of a non-desiccated Mediterranean Sea. Paleogeogr. Palaeoclimatol. Palaeoecol. 433, 201–218.

Lustrino, M., Wilson, M., 2007. The circum-Mediterranean anorogenic Cenozoic igneous province. Earth Sci. Rev. 81, 1–65.

Lyberis, N., Manby, G., 1999. Oblique to orthogonal convergence across the Turan Block in the post-Miocene. AAPG Bull. 83, 1135–1160.

Ma, S.S., Zhang, Q., Jin, W.J., 2017. A giant Eurasian Plateau of Miocene: Evidence from adakites. Bull. Mineralogy, Petrology Geochem. 36, 920–926 (in Chinese with English abstract).

Martínez, F., Parra, M., Arriagada, C., Mora, A., Bascuñan, S., Peña, M., 2017. Late Cretaceous to Cenozoic deformation and exhumation of the Chilean Frontal Cordillera (28°–29° S), Central Andes. J. Geodyn. 111, 31–42.

Meek A.S., 2014. Sandstone uranium deposits of Nebraska and Colorado: a comparative study. Ph.D. Thesis, University of Manitoba, Winnipeg, Manitoba, pp. 75. URI: http://hdl.handle.net/1993/23662.

Miller, K.G., Kominz, M.A., Browning, J.D., Wright, G.S., Mountain, M.E., Katz, P.J., Sugarman, B.S., Cramer, B.S., Christe-Blick, N., Pekar, S.F., 2005. The Phanerozoic record of global sea-level change. Science 310, 1293–1298.

Misra, S., Froelich, P.N., 2012. Lithium isotope history of Cenozoic seawater: changes in silicate weathering and reverse weathering. Science 335, 818–822.

Mougamba, R., 1999. Chronologie et architecture des systèmes turbiditiques cénozoïque du prisme sédimentaire de l'Ogooué (Marge nord-Gabon). Université de Lille 1, Villeneuved' Ascq 285.

Norris, R.D., Turner, S.K., Hull, P.M., Ridgwell, A., 2013. Marine ecosystem responses to Cenozoic global change. Science 341, 492–498.

Piedrahita, V.A., Bernet, M., Chadima, M., Sierra, G.M., Marín-Cerón, M.I., Toro, G.E., 2017. Detrital zircon fission-track thermochronology and magnetic fabric of the Amagá Formation (Colombia): intracontinental deformation and exhumation events in the northwestern Andes. Sed. Geol. 356, 26–42.

Piqué, A., Tricart, P., Guiraud, R., Laville, E., Bouaziz, S., Amrhar, M., Ait Ouali, R., 2002. The Mesozoic-Cenozoic Atlas Belt (North Africa): On overview. Geodin. Acta 15, 185–208.

Piquer, J., Hollings, P., Rivera, O., Cooke, D.R., Baker, M., Testa, F., 2017. Along-strike segmentation of the Abanico Basin, central Chile: New chronological, geochemical and structural constraints. Lithos 268–269, 174–197.

Placzek, C.J., Heikoop, J.M., House, B., Linhoff, B.S., Pelizza, M., 2016. Uranium isotope composition of waters from South Texas uranium ore deposits. Chem. Geol. 437, 44–55.

Potter, P.E., Szatmari, P., 2015. The global Middle and Late Miocene and the deep earth: Model for earlier orogenies. Mar. Pet. Geol. 68, 178–191.

Potter, P.E., Szatmari, P., 2009. Global Miocene tectonics and the modern world. Earth Sci. Rev. 96, 279–295.

Qian, Z.A., Song, M.H., Wu, T.W., Cai, Y., 2017. Review of advances in world dryland climate research: main investigation progress. Plateau Meteor 36, 1457–1476.

Ring, U., Gessner, K., Thomson, S.N., 2017. South Menderes Monocline: Low-temperature thermochronology constrains role of crustal extension in structural evolution of southwest Turkey. Tectonophysics 712–713, 455–463.

Rosenberg, P.E., Hooper, R.L., 1982. Fission-track dating of sandstone-type uranium deposits. Geology (Boulder) 10, 481–485.

Santos, E.S., Ludwig, K.R., 1983. Age of uranium mineralization at the Highland Mine, Powder River basin, Wyoming, as indicated by U-Pb isotope analyses. Econ. Geol. 78, 498–501.

Said, R., 1981. The geologic evolution of the River Nile. Springer Verlag, NewYork, pp. 151.

Sakai, T., Saneyoshi, M., Tanaka, S., Sawada, Y., Nakatsukasa, M., Mbua, E., Ishida, H., 2010. Climate shift recorded around 10 Ma in Miocene succession of Samburn Hills, northern Kenya Rift, and its significance. In: Clift, P.D., Tada, R., Zheng, H. (Eds.), Monsoon: Evolution and Tectonics, Geol. Society [London] Spec. Pub 342, 109–128.

Saucier, A.E., 1980. Tertiary oxidadon in the Westwater Canyon Member of the Morrison Formation, in C. A. Rautman, compiler. Geology and mineral technology of the Grants uranium region. New Mexico Bureau of Mines and Mineral Resources Memoir 38, 116–121.

Sclater, J.G., Meinke, L., Bennett, A., Murphy, C., 1985. The depth of the ocean through the Neogene. In: Kennett, J.P. (Ed.), The Miocene Ocean: Paleogeography and Biogeography. Memoir 163. Geological Society of America, pp. 1–19.

Sheahan, C., Fayek, M., Quirt, D., Jefferson, C.W., 2016. A combined ingress-egress model for the Kianna unconformity-related uranium deposit, Shea Creek Project, Athabasca Basin, Canada. Econ. Geol. 111, 225–257.

Song, Z.S., 2013. Metallogenic chronology and its geological significance in Hangjinqi sandstone-type uranium, Ordos Basin (Master's Dissertation). Northwestern University, Xi'an, pp. 32–39 (in Chinese with English abstract).

Spiegel, C., Kohn, B., Raza, A., Rainer, T., Gleadow, A., 2007. The effect of long-term low-temperature exposure on apatite fission track stability: a natural annealing experiment in the deep ocean. Geochim. Cosmochim. Acta 71, 4512–4537.

Thomson, Stuart N., 1994. Fission track analysis of the crystalline basement rocks of the Calabrian Arc, southern Italy: evidence of Oligo-Miocene late orogenic extension and erosion. Tectonophysics 238, 331–352.

Tinker, J., De Wit, M., Brown, R., 2008. Mesozoic exhumation of the southern Cape, South Africa, quantified using apatite fission track thermochronology. Tectonophysics 455, 77–93.

Van Ufford, Q.A., Cloos, M., 2005. The Cenozoic tectonics of New Guinea. AAPG Bull. 89, 119–140.

Vera, E.A.R., Mescua, J., Folguera, A., Becker, T.P., Sagripanti, L., Fennell, L., Orts, D., Ramos, V.A., 2015. Evolution of the Chos Malal and Agrio fold and thrust belts, Andes of Neuquén: insights from structural analysis and apatite fission track dating. J. S. Am. Earth Sci. 64, 418–433.

Vetrov, E.V., Buslov, M.M., De Grave, J., 2016. Evolution of tectonic events and topography in southeastern Gorny Altai in the Late Mesozoic-Cenozoic (data from apatite fission track thermochronology). Russ. Geol. Geophys. 57, 95–110.

Wagner, M., Altherr, R., Haute, P.V.D., 1992. Apatite fission-track analysis of Kenyan basement rocks: constraints on the thermotectonic evolution of the Kenya dome. A reconnaissance study. Tectonophysics 204, 93–110.

Walgenwitz, F.R., Richert, J.P., Charpentier, P., 1992. Southwest African platemargin: thermal history and geodynamical implications. In: Poag, C.W., Graciansky, P.C.D. (Eds.), Geologic Evolution of Atlantic Continental Rises. Van Nostrand Reinhold, New York, pp. 20–45.

Wang, E., 2013. Evolution of the Tibetan Plateau: as constrained by major tectonic thermo events and a discussion on their origin. Chinese J. Geol. 48, 334–353 (in Chinese with English abstract).

Wang, F.F., Liu, C.Y., Niu, H.Q., Zhou, N.C., Li, X.H., Luo, W., Zhang, D.D., Zhao, Y., 2018. In-situ chemical age of the sandstone-hosted uranium deposit in Ningdong area on the western margin of the Ordos Basin, North China. Acta Geologica Sinica (English Edition) 92, 406–407.

Wang, F.F., Liu, C.Y., Qiu, X.W., Guo, P., Zhang, S.H., Cheng, X.H., 2017. Characteristics and distribution of world's identified sandstone-type uranium resources. Acta Geol. Sin. 91, 2021–2046 (in Chinese with English abstract).

Wang, M.Q., 2017. Multi stage tectonic activation and uranium metallization in China. Uranium Geol. 33, 9–15 (in Chinese with an English abstract).

Wang, X., Zattin, M., Li, J., Song, C., Peng, T., Liu, S., Liu, B., 2011. Eocene to Pliocene exhumation history of the Tianshui-Huicheng region determined by Apatite fission track thermochronology: implications for evolution of the northeastern Tibetan Plateau margin. J. Asian Earth Sci. 42, 97–110.

Wang, Z.B., 2002. Current status and prospects of uranium geology developments of foreign in-situ leachable sandstone type uranium deposits. Uranium Geol. 18, 9–21 (in Chinese with an English abstract).

Wauschkuhn, B., Jonckheere, R., Ratschbacher, L., 2015. The KTB apatite fission-track profiles: building on a firm foundation? Geochim. Cosmochim. Acta 167, 27–62.

Whipple, K.H., 2009. The influence of climate on tectonic evolution of mountain belts. Nat. Geosci. 2, 97–104.

Wildman, M., Brown, R., Watkins, R., Carter, A., Gleadow, A., Summerfield, M., 2015. Post break-up tectonic inversion across the southwestern cape of South Africa: new insights from apatite and zircon fission track thermochronometry. Tectonophysics 654, 30–55.

Wilke, F.D.H., Sobel, E.R., O'Brien, P.J., Stockli, D.F., 2012. Apatite fission track and (U–Th)/He ages from the Higher Himalayan Crystallines, Kaghan Valley, Pakistan: implications for an Eocene Plateau and Oligocene to Pliocene exhumation. J. Asian Earth Sci. 59, 14–23.

Wu, F.Y., Liu, Z.C., Liu, X.C., Ji, W.Q., 2015. Himalayan leucogranite: Petrogenesis and implications to orogenesis and plateau uplift. Acta Petrologica Sinica 31, 1–36 (in Chinese with an English abstract).

Wülser, P.A., Brugger, J., Foden, J., Pfeifer, H.R., 2011. The Sandstone-Hosted Beverley uranium deposit, Lake Frome basin, South Australia: mineralogy, geochemistry, and a time-constrained model for its genesis. Econ. Geol. 106, 835–867.

Xia, Y.L., 2015. U-Pb isotope tracer in the mineralization of sandstone type uranium deposits. Acta Geological Sinica 89 (Supp.), 69–70 (in Chinese with English abstract).

Xia, Y.L., Lin, J.R., Li, Z.Y., Liu, H.B., Hou, Y.X., Fan, G., 2004. Study on geochronology of sandstone-type uranium mineralization in western Hailaer basin. Uranium Geol. 20, 146–150 (in Chinese with English abstract).

Xia, Y.L., Lin, J.R., Liu, H.B., Fan, G., Hou, Y.X., 2003. Analysis on metallogenic conditions and prospect prognosis for interlayer oxidation zone sandstone-type uranium deposit at western slope of Songliao basin. Uranium Geol. 19, 129–137 (in Chinese with English abstract).

Xiao, G.Q., Zhang, C.X., Guo, Z.T., 2014. Initiation of East Asian monsoon system related to Tibetan Plateau uplift from the latest Oligocene to the earliest Miocene. Chinese J. Nat. 36, 165–169 (in Chinese with English abstract).

Xiao, X.J., Li, Z.Y., Guo, H., Guo, Q.Y., 2003. The latest research achievements of sandstone-type uranium deposits in Russia. Uranium Geol. 19, 34–41 (in Chinese with English abstract).

Zachos, J., Pagani, M., Sloan, L., Thomas, E., Billups, K., 2001. Trends, rhythms, and aberrations in global climate 65 Ma to present. Science 292, 686–693.

Zhang, C., Yi, C., Dong, Q., Cai, Y.Q., Liu, H.X., 2018. Geological and geochronological evidence for the effect of Paleogene and Miocene uplift of the Northern Ordos Basin on the formation of the Dongsheng uranium district, China. J. Geodyn. 114, 1–18.

Zhang, J.D., 2016. Innovation and development of metallogenic theory for sandstone type uranium deposit in China. Uranium Geol. 32, 321–332 (in Chinese with an English abstract).

Zhang, M.Y., Zheng, J.W., Tian, S.F., Xia, Y.L., Liu, H.B., 2005. Research on existing state of uranium and uranium ore formation age at Qianjiadian uranium deposit in Kailu depression. Uranium Geol. 21, 213–218 (in Chinese with an English abstract).

Zhao, F.M., 2013. Central Asia institute of uranium. Beijing Research Institute of Uranium Geology, Beijing, pp. 1–373 (in Chinese without English abstract).

Zhao, L., Cai, C.F., Jin, R.S., Li, J.G., Li, H.L., Wei, J.L., Guo, H., Zhang, B., 2018. Mineralogical and geochemical evidence for biogenic and petroleum-related uranium mineralization in the Qianjiadian deposit, NE China. Ore Geol. Rev. 101, 273–292.

Zhou, K.K., Wu, H., Chen, X.W., Zhang, J.J., Xia, Y., 2017. Tectonic-basin evolution in Tengchong block, western Yunnan Province, and minerogenetic conditions of sandstone type uranium deposits. Geol. Bull. China 36, 541–546 (in Chinese with English abstract).

Zhu, Y.P., Gao, W.H., Ma, N., Kuang, F.X., Qiao, M.P., 2014. Metallogenic regionalization, deposit types and ore-search prospect for uranium deposits in Australia. Geol. Bull. China 33, 172–186 (in Chinese with English abstract).